

# Construction of a Semiconducting Three-Dimensional Polydimethylsiloxane (PDMS) and Hematite-Based Scaffold for use in Light Addressable Electrochemical (LAE) Imaging and Sensing

Third Year Project

Hannah Khan, Student ID: 190352587

BEng, Biomedical Engineering with Industrial Placement

Supervisor: Professor Steffi Krause

Date: 25/04/2023

SCHOOL OF ENGINEERING AND MATERIALS SCIENCE

ENGINEERING/MATERIALS

THIRD YEAR PROJECT

DEN318

APRIL 2023


DECLARATION

This report entitled

Construction of a Semiconducting Three-Dimensional Polydimethylsiloxane and Hematite Based Scaffold  
for use in Light Addressable Electrochemical Imaging and Sensing

was written by me and is my own work. Where the work of others has been used, I have fully acknowledged in the text, captions, tables, and illustrations. This report has not been submitted for any other qualifications.

Name: Hannah Khan

Signed: 

Date: 25/04/2023

## Acknowledgements

Thank you to my supervisor, Professor Steffi Krause whose patience, guidance, enthusiasm, and specialist knowledge helped guide me through this project. Thank you for always being available to help, for giving your time to explain unknown or difficult concepts, and for sharing your years of experience. Thank you for the weekly meetings that helped keep me on accountable throughout the year and for your moral and expert support. I am truly grateful for your coaching, feedback and guidance throughout this year.

Thank you to my post-doc guide, JiaZhe Zhou for your patience and support in organising and attending the many trainings required to complete the experimentation in this report. Thank you for the moral support, camaraderie, knowledge transfer and problem-solving attitude that helped me keep a cool head and build my resilience throughout this project. Thank you for giving your time, no matter the day or hour, to answer my questions and coach me through my own problem-solving issues. I truly value the partnership and mentor ship that you have provided that helped me develop my laboratory skills and experimental awareness.

Thank you to Dr. Bo Zhou for sharing your patience, training, and expert knowledge in hematite fabrication and in understanding the Light Addressable Electrochemical Imaging processes.

Thank you to Dr. Jose Serrano for providing lengthy 2-point and 4-point probe training, data collection, and for the PEDOT:PSS recommendation. Despite not being in the same research group, I thank you for your patience in indulging my many questions.

Thank you to Stefano Ahwulia for your patience, support and for providing the freeze dryer training. Thank you for the camaraderie and life advice you've provided throughout the project duration.

Thank you to the many post-doc fellows and Dr.s who provided great motivational and emotional support, time and patience throughout this project.

## Contents

Abstract.....	5
Abbreviations.....	6
List of figures.....	7
1. Introduction .	8
1.1.    2D vs 3D Tissue Engineering .....	8
1.2.    Principles of Light Addressable Electrochemical Imaging (LAEI) and Electrodes (LAE) .....	8
1.3.    Semiconductor Substrates Employed for LAE.....	10
1.4.    Applications of LAE in Cell Analysis.....	11
1.5.    Scaffold Templating Techniques .....	11
1.6.    Project Aims .....	12
2. Sample Preparation .....	12
2.1.    Materials and Instrumentation.....	12
2.2.    Blend composition tables.....	13
2.3.    Experimental Preparation Methods.....	14
3. Results and Discussion .....	15
3.1.    Experiment 1 – PDMS: Hematite Films .....	15
3.2.    Experiment 2 – PEDOT:PSS and Hematite Film.....	21
3.3.    Experiment 3 – PDMS: ITO Concentration Series .....	24
3.4.    Experiment 4 – Gelatin Scaffold Templating .....	28
4. Conclusion.....	29
Bibliography .....	31

## Abstract

This report explored the fabrication of a macroporous, three-dimensional scaffold from a range of organic, inorganic, conductive and semiconductive materials for use in photoelectrochemical analysis and live LAE imaging. The material blends underwent conductivity and photocurrent testing and comparisons to determine the best blend for this live imaging application. Through vigorous experimentation, it was found that a PEDOT: PSS and hematite film outperformed all other samples in electrical conductivity, however its volatile and degenerative nature under applied conditions makes it unreliable. Therefore, an inorganic alternative was found through a PDMS: ITO concentration series which produced the second highest (to PEDOT: PSS) electrical conductivity and lowest film resistance at 70%, that can withstand higher voltages than the PEDOT: PSS film. A simple, layered porous gelatin scaffold was also fabricated to act as a scaffold template with the chosen optimum blend, providing a template for further experimentation and eventual cardiomyocyte cell culture. The application of a semiconductive LAE imaging scaffold has greater applications for biological tissue analysis in testing drug delivery systems and developing organ-on-a-chip technologies.

## Abbreviations

BG: Band gap

CNT: Carbon Nano Tube

EC: Electrical Conductivities

EL: Energy Levels

eS: Electron shells

eV: Electron Volts

ICSD: Inorganic Crystal Structure Database

ITO: Indium Tin Oxide

LAE: Light Addressable Electrodes

LAEI: Light Addressable Electrochemical Imaging

LAPS: Light Addressable Potentiometric Sensor

OOAC: Organ-on-a-Chip (technology)

PD: Potential Difference

PBS: Phosphate Buffered Saline (solution)

PD: Potential Difference

PDMS: Polydimethylsiloxane

PEDOT: PSS : Poly(3,4-ethylenedioxythiophene) : Polystyrene Sulfonate

PEO: Polyethylene oxide

SECM: Scanning Electrochemical Microscopy

SOS: Silicon-on-Sapphire

SPE: Single Photon Excitation

TC: Tissue Culture

TE: Tissue Engineering

TPE: Two Photon Excitation

2D: Two Dimensional

3D: Three Dimensional

## List of figures

Figure 1: Technical set up of photoelectrochemical imaging constructed by Professor Steffi Krause's research group in Zhou, et al. 2021, section 2.1 of the report .....	9
Figure 2: summarised schematic of the project process in fabricating a semiconductive 3D scaffold .....	12
Figure 3: Schematic of hematite synthesis process .....	15
Figure 4: Nine PDMS based samples were made from a range of Hematite, Hematite/ITO and Hematite/CNT compositions .....	16
Figure 5: ITO (11-18%) and Hematite (4-6%) films tested at an applied voltage of -10V to +10V at 21 steps on an axis of current vs voltage. ....	18
Figure 6: Films from ITO and Hematite, -10V to +10V at 21 step counts. ....	18
Figure 7 (above left): EC of ITO films (11-18%) and Hematite films (4-6%) compared via bar chart .....	20
Figure 8 (above right): Resistivities of ITO films (11-18%) and Hematite films (4-6%) compared via bar chart .....	20
Figure 9: Comparison of films' resistances across ITO films (11-18%) and Hematite films (4-6%) .....	20
Figure 10: XRD data for the hematite used in the PEDOT: PSS and hematite film compared to a standard peak values checking if the particles contained hematite crystals or not. The comparison shows the presence of hematite crystals in the red powder tested. ....	22
Figure 11 (0.1-15 V): 4-point probe conductivity testing of 14% hematite and PEDOT: PSS film with an applied voltage range of 0.1 V -15 V .....	22
Figure 12: 4-Point probe conductivity testing of 14% hematite and PEDOT: PSS film with applied voltage range of 0.1 V-1 V, focusing on the film's behaviour at smaller voltages .....	22
Figure 13: ECs of PEDOT: PSS + hematite film compared to the calculates EC of PEDOT: PSS only, via bar chart .....	23
Figure 14: Resistances of PEDOT: PSS + hematite film measured at 1V and averaged, absolute values compared via bar chart .....	23
Figure 15: Current/Voltage graph of PEDOT: PSS + hematite film tested photoelectrochemically via Linear Sweep Voltammetry and collected virtually using AutoLab .....	24
Figure 17: ITO concentration series (with carbon contacts), spin-coated film samples of SYLGAD 180 PDMS and curing pack (0.1g) dissolved in Hexane (1 mL), with varying concentrations of dispersed ITO on plasma treated 1cm x 1cm glass squares, with carbon paste contacts templated onto the films for improved electrical contact testing with the 2-point probe, barring the sample at 70% ITO composition .....	25
Figure 16: ITO concentration series (without carbon contacts), spin-coated film samples of SYLGAD 180 PDMS and curing pack (0.1g) dissolved in Hexane (1 mL), with varying concentrations of dispersed ITO on plasma treated 1cm x 1cm glass squares. ....	25
Figure 18: 5V with Carbon contacts at 21 steps. ....	26
Figure 19: Graph of electrical conductivity calculated from Table 8 against ITO percentage concentration, comparing conductivities of each film. ....	27
Figure 20 (above left): Light microscope image of piled dry gelatin particles at 250-300 $\mu\text{m}$ . ....	29
Figure 21 (above right): Microscope image of porous sintered gelatin particles (250-300) $\mu\text{m}$ after saturation with 40 microlitres of ethanol solution (vol/vol 85%) with Ultra-Pure water. Sintered at 60° for 20 mins. ....	29
Figure 22 (above left): Gelatin particle piles pre-heating in oven at 40° for 8 hours .....	29
Figure 23 (above right): Gelatin, post-heating in oven at 40 for 8 hours. Particles has melted into a film instead of sintering into a scaffold .....	29
Figure 24: EC comparison via bar chart of the best performing films from experiments 1-3 .....	30

# 1. Introduction

## 1.1. 2D vs 3D Tissue Engineering

In vitro biomedical research models provide safe environments to test and analyse patient reactions to new treatment methods. Common examples of these models are drug delivery systems in the pharmaceutical industry; however, efforts have been made to expand the variety of models available that accurately replicate and mimic human physiological responses within the field of personalised medicine [25].

Current models utilise 2D Tissue Culture (TC) to analyse the cellular and tissue response to 1) changing internal and external physiological environments, 2) responses to the applied treatment and 3) to analyse the effect of intercellular communication pathways on tissue phenotype, morphology, and viability. 2D TC is conducted on a flat plane, where fresh media is switched out at regular intervals to increase the tissue viability, access to nutrients and removal of waste products. However, research has shown that 2D TCs are not representative of the cellular interactions that occur in hierarchical organisms, where their cells operate in a 3D physiological environment [1].

As a result, 3D Tissue Engineering (TE) arose as a solution to 2D TC limitations, evolving the planar growth into 3D scaffolds for use in bioreactors, adapting the materials, topography, and structure (porosity) to replicate cellular ECM. This develops vascular systems for systemic nutrient diffusion and waste removal, providing an environment for 3D intercellular communication – of which there is limited understanding of the importance of neighbouring cells' impact on cell lineage, creating the potential to better tailor cellular differentiation and therefore, specific tissue development through environmental controls.

## 1.2. Principles of Light Addressable Electrochemical Imaging (LAEI) and Electrodes (LAE)

Optical imaging is an essential analysis tool used in biomedical and materials research. The ability to image samples to the micro- and nano-levels at high resolutions introduces an improved understanding of material topography, molecular interactions and chemical activity of biological tissue or materials in the imaging environment. Various forms of optical imaging utilise light to live image or scan samples in microscopes like scanning electrochemical microscopy (SECM) that enables high spatial mapping of biological tissues' surfaces and chemical activities using an automated redox-sensitive probe to collect live data on the volume of redox species present on the sample's surface tested at the time [4]. According to Conzuelo et al., 2010, the scanning process occurs in a single 2D where live optical images of the sample's surface and chemistry are created based on the redox reaction data generated by a microcurrent at the tip's surface (Introduction). The report discusses limitations of the scanning technique like distance between the probe tip and sample, the speed and force the tip was moved across the sample – as it should be moved gently - to ensure accurate and clearly defined imaging without damage to the instrumentation. However, experimental research has been conducted to address these issues, resulting in constant-distance mode cellular SECM which measured cell topography at greater resolutions and provided insight into single planar cellular response to live stimulation [4].

Bioanalytical imaging processes like SECM are paired with an optical imaging labelling technique like confocal microscopy [5, 17, 21], which is known for its wide-field, high-resolution and fast live-cell fluorescence imaging in



biomedical research. The application of dyes helps isolate and identify desired structures in a 2D optical image. However, issues associated with fluorescence labelling techniques ranging from phototoxicity and bioleaching from the dyes to the high-powered lasers used to illuminate samples that can damage the cells [5]. All which affects the quality and reliability of the data produced thereby making it necessary to seek out less invasive and label free live-imaging alternatives.

An alternative is light addressable electrodes (LAE) used by Zhou et al., 2021 their non-contact photoelectrochemical imaging of 2D in-vitro cell cultures on thin semiconductive hematite films. In this paper, Zhou et al., 2021 generated a photocurrent using a semiconductor electrode/electrolyte circuit to obtain high resolution spatial images of localised cross-sections on a hematite semiconductor substrate in film and nanorod form. The technical set up is shown in Figure 1 with accompanying description described in Zhou et al., 2021, section 2.1. Light addressable electrochemical imaging (LAEI) with

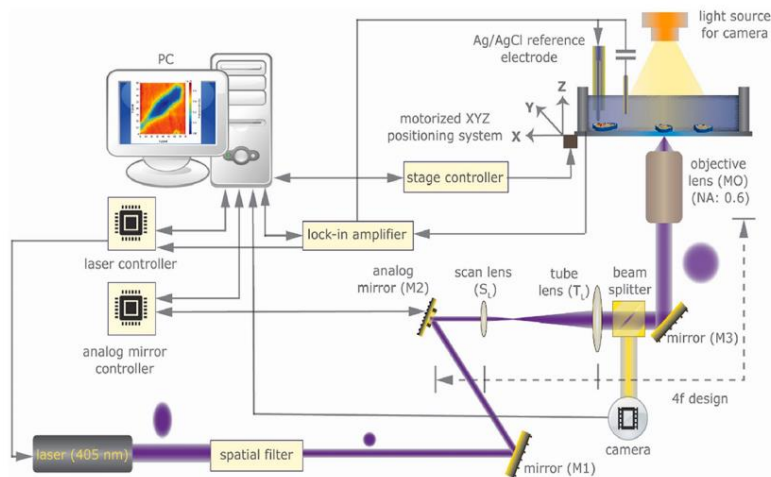


Figure 1: Technical set up of photoelectrochemical imaging constructed by Professor Steffi Krause's research group in Zhou, et al. 2021, section 2.1 of the report

LAEs, use band bending, electron excitation and redox reactions at the semiconductor electrode/electrolyte interface to generate a photocurrent in the sample. In semiconductors, a band gap occurs between the valence (lower) and conduction (higher) bands, corresponding to a particular voltage (electron volts – eV) detailing the excitation energy required for an electron- hole pair to form from the promotion of an electron to the conduction band, leaving a hole in the valence band. N-type semiconductors, like hematite [11, 13, 26] have an abundance of electrons to be promoted across the gap allowing the flow of current through the substrate. The electrons on the valence bands do not have enough energy to pass this band gap individually, therefore an external thermal or light energy is required for electron promotion. An applied voltage bias induced electrical band bending in the semiconductor through an electric field pushing charge carriers (electrons) into the semiconductor bulk and depleting the band region at the semiconductor-electrode surface. This accumulates positively charged minority charge carriers (holes) at the surface on the valence band, due to the direction of band bending.

When redox energy levels of the electrolyte solution fall between the band gap of an n-type semiconductor, oxidation reactions occur at the electrode/electrolyte interface where the holes from the semiconductor react with the electrons from the solution species until an equilibrium transfer is met. This generates a so-called dark current causing an increase in positive potential difference (PD) separate from the applied bias voltage. Equilibrium occurs when the redox energy level and the semiconductor's fermi level equalise, level with the bent conduction band. When the semiconductor is illuminated in addition to the applied voltage, a region of high conductivity occurs as more electron-hole pairs form, increasing the redox reactions, causing a sharp increase in PD away from the dark current described

as a local DC photocurrent, where these changes in potential difference are digitally measured on a spectrometer graph analysed by a computer software [26].

The laser can be applied in single and two photon effects, where both techniques provide the energy to promote an electron through the absorption of a single or two photons. Chen et al., 2010 measured photocurrent of silicon-on-sapphire (SOS) substrates using a two-photon excitation (TPE) with Light Addressable Potentiometric Scanning, to achieve high spatial resolution of laterally imaged SOS substrates by measuring the generated photocurrent as a laser is applied to cross-sections across its surface. TPE provides advantages over Single Photon Excitation (SPE) by being less invasive and damaging to the samples by using a smaller wavelength, particularly if the samples are organic or biological (CytoSmart, n.d.). Chen et al., 2010 found that TPE provides small-field depth imaging at the laser focal point, as two photon absorbance can only occur at a point of high photon density, providing images of greater resolution and depth than by which SPE provides which is wide-field as all photons applied from the laser have enough energy to excite multiple electrons to the conduction band at all points of illumination in the semiconductor's bulk and not just in the laser focus. TPE therefore uses light energy with smaller wavelengths than the semiconductor's band gap, to limit the amount of sample surface area that is photoelectrochemically activated and imaged. Additionally, Furey et al., 2022 states that for good two photon absorbance and high spatial resolution of thin films to occur, it was necessary to include a good insulator and electrolyte with a strong oxide to achieve an efficient photocurrent. Polydimethylsiloxane (PDMS) is a silicone polymer used throughout healthcare in biomedical implants for its stable and biocompatible structure and ability to mimic the mechanical properties of extracellular matrices [14]. It has been used in Xu et al., 2020 to create a microporous orbital implant in rabbits with great success.

### 1.3. Semiconductor Substrates Employed for LAE

The type of substrate used in LAE imaging is important to consider when defining your project to produce a viable and good photocurrent. There's a great deal of photocurrent testing in the fields of renewable energy [11] and biomedical research with thin electrode films for live high spatial resolution imaging in biomedical research [6, 26]. A common substrate used in these papers was hematite, described as a highly stable form of iron oxide n-type semiconductor known for its non-toxicity, abundance, and a good band gap position of approximately 1.9-2.1 eV [26] that can adsorb almost 40% of solar energy [11]. Zhou et al., 2021 tested both ITO and hematite substrates in both LAPS and LAE experiments, discovering that the latter produced a photocurrent '18 times larger' (Introduction) than ITO at half the working voltage, making it the better choice in analytical biological imaging and clean energy research.

Liao et al., 2011 found that Pure hematite can oxidise water to make oxygen alone but can only reduce water to make hydrogen with an applied electrical bias. Whereas doped hematite could do so without the need of external electrical bias. All three articles mentioned that (pure) hematite naturally has very low conductivity, low motility of charge carriers and minority carries, (high resistance to movement) and high rates of electron-hole recombination due to the charge carriers' short lifetimes. Li et al., 2018 and Lia et al., 2011 suggested that hematite conductivity could be improved via doping (usually substitutional) with Liao et al., 2011 conducting experimental testing that found the best doping materials to enhance the n-type semiconductive of pure hematite without increasing resistance to mobility of

charge molecules were zirconium, silicon and germanium. Silicon itself has been used in many photoelectrode/photoanode studies in renewable energy, particularly the silicon on sapphire substrates mentioned previously [6], that developed these samples for two photon excitation in LAPS and SICM.

#### 1.4. Applications of LAE in Cell Analysis

Photoelectrochemical imaging is useful in the study of biological systems, however, current imaging of cellular activity is limited to 2D planar external-surface measurements of interactions with neighbouring cells in a low biomimetic, in-situ environment like 2D tissue cultures on semiconductive, biocompatible films [3, 4, 6, 17, 26]. The ability to live image cellular processes beyond a surface understanding of cell membrane activity in a 3D biophysiological environment would be a coveted process in biomedical research. It would unlock specific, enhanced understanding of molecular processes inside-outside and during transportation, changes to surface charges because of these processes and the effect that similar, neighbouring electrochemical cell activity could have on cell lineage and differentiation. It would also allow more accurate spatial resolution mapping of surface topographies and charge, for specific analysis of multiple behavioural cellular responses to external stimuli like local changes in pH, temperature or nutrient concentration, or the effect of clinically trialled drugs new drugs in the field of personalised medicine [25].

#### 1.5. Scaffold Templating Techniques

Microporous PDMS scaffolds were developed through a gelatin templating and porogen leaching method [24]. Gelatin particles were sintered in separate hemispherical moulds before being joined together to create an orbital implant tested in rabbit eye-sockets. PDMS was chosen for the scaffold and the rabbits' host response measured to the implant. Xu et al., 2020 found that PDMS created a better successful, biocompatible implant with the required elastic properties to act as a matrix for cell seeding and tissue regeneration.

The application of ice templating into tissue engineering research has great future potential in fabricating microporous 3D scaffolds from biopolymer and live cell-based blends [18]. They state that ice templating is traditionally used to mould and set materials with defined properties like porosity and stiffness. Useful in industry with the generation of ceramics, and in templating hydrogel scaffolds made from gelatin, chitosan, or alginate. Ice templating uses thermal gradients to generate a unilateral growth of solvents ice-crystal rods through a material or suspension (at room temperature) when in contact with another (cold/freezing) surface. Water is the most common solvent used in ice templating, for its agile thermal phase properties and easy removal without the addition of a secondary solvent to leach it from the set template. However, as with any process, ice templating is limited by certain factors shared like porosity and pore size are affected by properties like geometry, sample volume, freezing rate and stability of biological materials like collagen, especially when maintaining cell viability [18]. Where control over local thermal gradients throughout the sample is more difficult to isolate than the sample's overall gradient thereby potentially resulting in some non-uniformity in ice rod size and growth depth, affect template's porosity and pore sizes.

Another templating technique used is electrospinning, which creates a 3D network of fibres rotated in an electric field to generate scaffolds with larger surface areas than 2D surfaces. This increases the amount of semiconductive substrate in contact with the electrolyte for their photoelectrochemical measurements of their electrode template -

made from a blend of polyethylene oxide (PEO) and ITO nanoparticles [15]. These complex structures can be tailored for experimental analysis, as fibre diameters and lengths can be adjusted for personalisation, eg. fibres with diameter ranges of 10 $\mu$ m – 10nm, and the duration of electrospinning affecting scaffold size. The longer the material is spun, more ink enters the magnetic field and is increasing incorporated in the continuously forming scaffold. generated resulting in an increasing mass of fibres in the scaffold.

## 1.6. Project Aims

Inspired by two core research articles in from sections 1.1-1.5 (Zhou et al. 2021 and Xu et al. 2020) this project aims to fabricate a semiconductive film using different compositions of PDMS, hematite synthesised from research [26] and whilst exploring alternative materials combinations. Thin glass films of each fabricated sample will be tested for conductivity and resistance through a 2-point or 4-point probe and if successful, they will be photoelectrochemically tested for a photocurrent using the LAE set up in Figure 1, section 1.1.

For the 3D scaffold template, Xu et al. 2021's methodology will also be adapted to fabricate a multi-layered flat gelatin scaffold as a template for the optimum semiconductive blend.

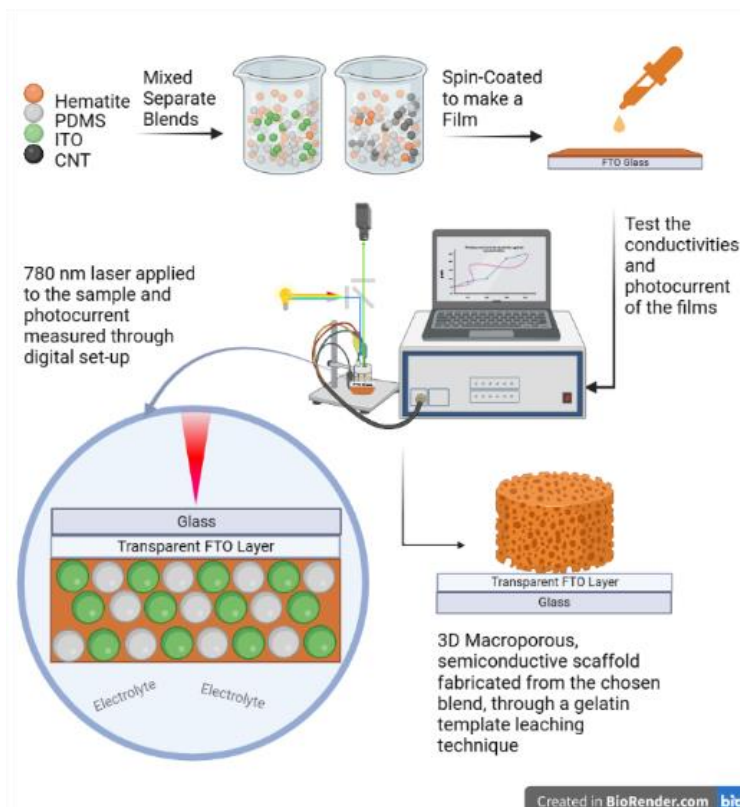


Figure 2: summarised schematic of the project process in fabricating a semiconductive 3D scaffold

## 2. Sample Preparation

### 2.1. Materials and Instrumentation

Table 1: Project Materials and Instrumentation

<b>Materials</b>	<p>Fluorine-doped tin oxide (FTO) coated glass (15 <math>\Omega</math>/sq.) and glass microscope slides were purchased from SigmaAldrich. To synthesise the HNR - Iron(III) chloride hexahydrate (<math>\text{FeCl}_3 \cdot 6\text{H}_2\text{O}</math>, ACS reagent, 97%) and sodium sulfate (<math>\text{NaSO}_3</math>, <math>\geq 99.0\%</math>), and all other chemicals not defined were purchased from SigmaAldrich. To make the silicone films - SYLGARD®184 (high molecular weight, clip pack with curing agent), ITO (<math>\text{In}_2\text{O}_5/\text{SnO}_2</math> Nanopowder, &lt;50 nm particle size) and single walled CNTs (<math>\geq 90\%</math> carbon basis, <math>\geq 80\%</math> as carbon nanotubes) were also purchased from SigmaAldrich. To make the porous gelatin template, gelatin from bovine skin (type B, powder, BioReagent) and fine test sieves (Brass, pore size 250 <math>\mu</math>m and Stainless Steel frame, pore size 300 <math>\mu</math>m) were purchased from SigmaAldrich.</p> <p>To make the PEDOT:PSS and Hematite film, PEDOT:PSS Solution (PH 1000, 1.0-1.3 wt.% in water) was bought from Ossila. And all other chemicals were purchased from SigmaAldrich.</p>
------------------	---

<b>Instrumentation</b>	Thermo scientific heratherm oven. Furnace – Carbolite. Bruker Dektak XT stylus Profilometer (SURFACE PROFILOMETER). Magnetic spin thing hot plate - Fisherbrand™ Isotemp™ Hot Plate Stirrer, Ambient to 540°C, Ceramic. Spin coater – Specialty Coating Systems, G3 Spin Coater Series. Pipette – Eppendorf® Research® plus Pipette Variable volume (10-100µL pipette). Scanning Electron Microscope – FEI Inspec-S Scanning Electron Microscope . Scan-Vac Coolsafe 110-4 pro Freeze dryer. Ceramic Crucible. Plasma treater. 100 mL Stainless Steel Hydrothermal Autoclave Reactor. Sonicator –. Ultrasonicator UltraWave Limited. Fine Test Sieves, Sigma Aldrich (250 µm and 300 µm). Thermo. Scientific Heraeus X1R Centrifuge. Optical microscope, Leica DFC420 C. SARTORIUS Practum Analytical Balance. Ossila four-point probe and two-point probe
------------------------	--

## 2.2. Blend composition tables

Table 2: Blend compositions for experiments in this report (3 sig. fig.)

Experiment 1 - PDMS: Hematite films with ITO or CNT						
	<i>PDMS (g)</i>	<i>Curing agent (μL)</i>	<i>Hematite addition (g)</i>	<i>Addition (g)</i>	<i>Composition of Hematite (%)</i>	<i>Composition of Addition (%)</i>
Hematite	0.1	0.01	0.0035	x	3.08	x
	0.1	0.01	0.007	x	5.98	x
	0.1	0.01	0.005	x	4.35	x
Hematite + ITO	0.1	0.01	0.005	0.025	3.57	17.9
	0.1	0.01	0.005	0.0135	3.89	10.5
	0.0991	0.01	0.005	0.0185	3.77	14.0
Hematite + CNT	0.1	0.01	0.005	0.0016	4.29	1.37
	0.1	0.01	0.005	0.0009	4.31	0.78
	0.1	0.01	0.005	0.0013	4.30	1.12
Experiment 2 - PEDOT: PSS + hematite film						
<i>Hematite (g)</i>	<i>PEDOT: PSS Solution (PEDOT: PSS + 30% H<sub>2</sub>O) (g)</i>			<i>PEDOT: PSS (g)</i>	<i>Composition of Hematite in the film (%)</i>	
0.0574	0.501			0.351	14	
Experiment 3 - PDMS: ITO films.						
Concentration series using 0.1g PDMS dissolved in 1mL of Hexane						
<i>Solid composition (%)</i>	30	40	50	60	70	80

ITO (g)	0.0429	0.0667	0.100	0.150	0.233	0.400
<b>Experiment 4 – Gelatin Scaffold Templates</b>						
<i>Gelatin particles (g)</i>			<i>Ethanol solution (μL)</i>			
0.02			40			

## 2.3. Experimental Preparation Methods

*Table 3: Experimental Preparation Methods*

Hematite Nanorod Preparation method	The experimental Hematite Nanorods (HNR) fabrication method was adapted from <a href="#">Zhou et al.</a> The schematic (Figure 3) illustrates the step-by-step process. To make approximately 0.15g of hematite, iron(III) chloride hexahydrate (0.81 g) and sodium sulfate (2.1 g) were magnetically stirred at a low temperature in 50 mL of ultra-pure water at a range of 130-300 rpm until dissolved. The solution was sealed into a 100 mL teflon-lined, stainless-steel autoclave and heated in an oven to 120°C for 12 hours to undergo a hydrothermal reaction. The hydrothermal product was then centrifuged at 4°C for 30 mins at 8000rpm, the supernatant was removed, and the product washed in ultrapure water, sonicated for 15 mins for re-dispersion and centrifuged again. This was repeated twice more, washing the centrifuged product with both ethanol and Ultra-Pure water at these separate intervals. After the final centrifugation and removal of the ultra-pure water supernatant, the hematite precursor product was freeze-dried for a maximum of 7 hours, giving rise to a brown/orange powder of FeOOH. This powder was transferred to a ceramic crucible and placed in a furnace to be heated to 520°C at a ramping rate of 10°C/min, and then kept at 520°C for 8 hours. The final form of HNR ( $\alpha$ -Fe <sub>2</sub> O <sub>3</sub> ) were obtained from the post-furnaced product.
Experiment 1 – PDMS: Hematite and ITO or CNT	Glass slides, cut to 1 cm x 1 cm squares, was sonicated in an ultrasonic bath to clean them in a mixture of acetone and ethanol for 15 mins. They were blown with dry with Nitrogen gas. 10-100 μL pipette with the pipette tip used to mix the materials in the weighing boat before using the tip to scoop the blend onto the glass squares and spreading it as evenly as possible before spin coating at 1400 rpm for 10 seconds. Made on approx. 1cm x 1 cm glass squares.
Experiment 2 – PEDOT: PSS and Hematite Nanorods	Glass and FTO Glass were cut into 1.2 cm x 1.2 cm squares and cleaned in the ultrasonicator (UltraWave Limited) for 15 mins in equal volume mixture of IPA and Acetone They were blown dry in pure Nitrogen and their surfaces etched in a Piranha solution (3:1 of sulfuric acid and hydrogen peroxide) for 1 min, to reduce their surface tension for a more even film when spin-coating the PEDOT: PSS and Hematite blend. After which they were washed thoroughly with ultra-pure water and blown dry with pure Nitrogen. Hematite and PEDOT: PSS solution were combined in an approximate weight to weight ratio of 1:6 yielding a hematite percentage of 14% of the film (Table 2). The mixture was ultrasonicated for 1 hour at 15-min intervals. The water in the bath was changed with fresh water after each interval with water that was kept cooled in the fridge/freezer as PEDOT: PSS was kept refrigerated and had a risk of degeneration in the warmed water. After sonicating, 40 μL of the



	dispersed blend was pipetted on the etched glass and FTO glass, squares, and spin coated at 1700 rpm for 10 seconds to obtain a thin film with a good balance between opaqueness and transparency. Finally, the spin-coated samples were cured on a hot-plate (Fisherbrand™ Isotemp™ Hot Plate Stirrer, Ambient to 540°C, Ceramic) for 30 mins at 140°C.
Experiment 3 – ITO Concentration Series	6 samples of PDMS: ITO films were made ranging from 30-80% ITO. Glass was cut into 1 cm x 1 cm slides and cleaned in the ultrasonicator for 15 mins in equal volumes of acetone and IPA and blown dry in nitrogen gas. The glass squares were plasma treated and left until needed. 0.1g PDMS and curing agent was dissolved in 1mL of hexane and mixed with measured ITO nanoparticles corresponding to make up the percentage range. The mixture was sonicated for 2 hours to achieve uniform dispersion. The dispersed mixtures were pipetted or spread, depending on their state, onto plasma treated glass squares before spin-coating for 10 seconds at 1400rpm.
Experiment 4 – Gelatin Scaffolds	Bovine gelatin particles (purchased from Sigma Aldrich) were separated through micro sized sieves to isolate particles of the size range 250-300 µm. 0.02g of the sieved particles were piled onto glass slides at 1.5 cm x 1.5 cm. An 85% ethanol solution was made from water and ethanal, and 40 µL added to each pile until submerged. The particles were sintered in solution on a hot plate at 60°C for 20 mins to create a porous gelatin template.

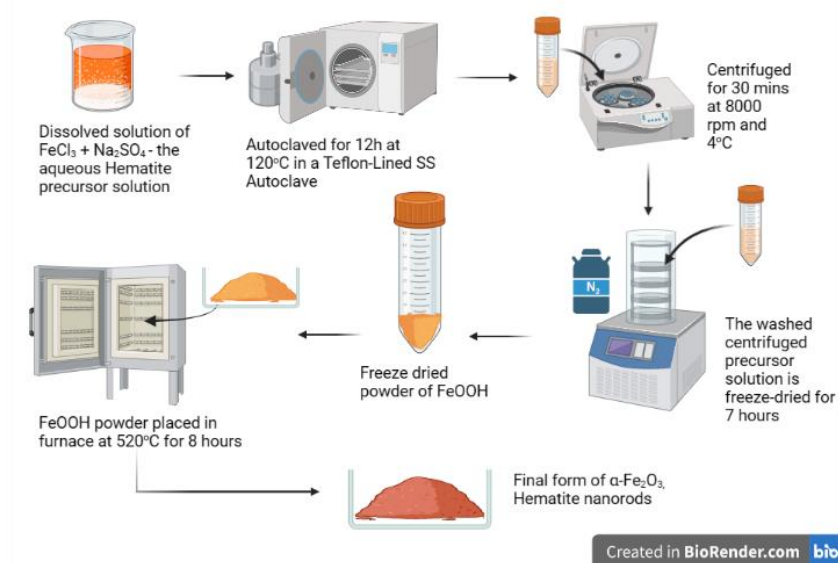


Figure 3: Schematic of hematite synthesis process

### 3. Results and Discussion

To achieve this project's aims, four experiments with varied material combinations - PDMS: HNR + ITO or CNT; PEDOT: PSS + HNR, and a PDMS: ITO – testing for good conductivity and material properties to generate an efficient photocurrent from LAE analysis.

#### 3.1. Experiment 1 – PDMS: Hematite Films

Experiment 1 builds on previous work in this research group/area (Zhou 2021) where aqueous hematite precursor, doped with tin was electrodeposited to make semiconductive 2D films which successfully generated a photocurrent

at. This experiment aimed to see if a photocurrent could also be generated from a blend of hematite and insulating polymer. Xu et al., 2020 used PDMS to construct their orbital implant due to its industry grade biocompatibility [14] so it was chosen as a medium to disperse HNRs and a conductive additive Indium Tin Oxide (ITO) or Carbon Nanotubes (CNT).

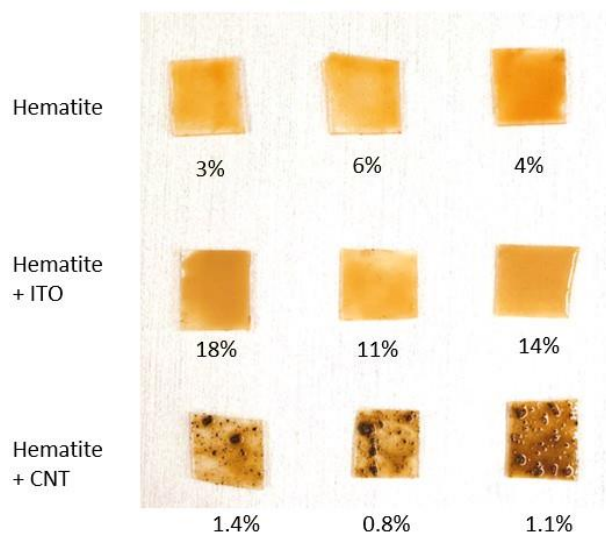


Figure 4: Nine PDMS based samples were made from a range of Hematite, Hematite/ITO and Hematite/CNT compositions.

Nine PDMS, Hematite and CNT films were prepared by weight based off the blend compositions in Table 2. They were spin-coated onto glass squares (1cm x 1cm) for conductivity testing by a commercially available two-point probe.

Figure 4 shows non-uniform films in all sample sets with varying thickness, dispersion of hematite, ITO or CNT, and sample volumes. The unequal volume distribution across the three samples were due to viscosity issues when pipetting the SYLGARD®184 PDMS. Its high viscosity at 3.5 Pa.s [22] made it stick to the pipette walls and would not be ejected onto the glass surface, either when using  $\mu\text{L}$  pipettes (10-100  $\mu\text{L}$ ) or disposable plastic (3 mL). This prevented equal

volumes of the elastomer to be transferred from the commercial packaging for weighing and mixing, resulting in the varied film appearances. This also affected the comparability of the samples due to the lack of control factors, as the methods used to generate these films in Figure 4 did not use standard practice which also affecting the reproducibility of this experiment.

Figure 4 shows the CNT samples with films that were darker in colour compared to the hematite and hematite + ITO films. This was a concern as a PDMS was chosen for its transparent fluid and to allow as much transparency as possible when used in photoelectrochemical imaging. Figure 4 shows that the hematite dispersed well into the PDMS but the CNTs aggregated into clumps due to the van-der-Waals forces between the nanoparticles, as found by Ranjendran et al., 2022 with their study into CNT dispersion in polar and non-polar solvent. They found that CNTs dispersed better in solvents with increasing polarities as the solvents' functional groups ( $-\text{COOH}$ ,  $-\text{OH}$  or  $\text{NH}_2$ ) form hydrogen, polar-polar bonds, with the CNTs [19, p.1]. The formation of these intermolecular bonds stabilises the position of the CNTs in the solvent, effectively repelling the CNTs from each other, improving their dispersion in a medium. However, given the non-polar characteristic of PDMS and opposing CNT polarity, a uniform dispersion of CNTs did not occur as these polar-polar bonds were not able to form. This caused the CNTs to repel and re-aggregate into different sized clusters that attempted to reduce their surface energy by grouping together, whilst also having a have a high surface area so they had absorbed the hematite in the mixture onto their surface, making even larger clusters.

The mass of PDMS did not affect the level of dispersion given the presence of clumps in all three samples. Therefore, CNT were found to be an inadequate additional conductive substance to the PDMS and hematite films due to its



opacity and lack of dispersion due to opposing polarities between CNTs and PDMS as shown in Figure 4, with ITO chosen as the additional conductive substrate over CNTs. They were therefore excluded from any further testing; instead, all ITO + hematite films (11% -18%) and hematite samples 6% and 4% (Figure 4), were tested for resistance and conductivity using a commercially available 2-point probe. Voltage ranges from 5-20V were applied to the films and representative graphs chosen for this results section to demonstrate the methodology in calculating the electrical conductivity of the best ITO and hematite samples out of the chosen population. Higher voltages were necessary to reduce the noise present at lower voltage ranges, creating more linearly defined and ohmic graphs to accurately calculate the films' resistances from.

The conductivity and resistance measurements from the 2- point probe was analysed where the below equations [7] were used to find the films' conductive properties. The probes base their data analysis on Ohm's law, eq. 1, where V – voltage (V), I – current (A) and R – resistance ( $\Omega$ ).:

$$\text{Voltage, } V = IR \quad (1)$$

To find resistance, Ohm's law (eq. 1) was rearranged to make R, the subject of the equation in eq. 2.

$$\text{Resistance, } R = \frac{V}{I} \quad (2)$$

Next to find the resistivity, the resistance found from eq. 2 was multiplied by the sample's width (w) and thickness (t), divided by the sample length (l) in eq. 3. Eq.3 was adapted from Heaney 2003, p. 4 to suit a uniform square sample instead of the rectangular sample used in their analysis. Due to the samples in this report being made into square films where the width and lengths are equal, they cancelled out leaving only the resistance multiplied by the film's thickness which was converted into cm for accurate calculation purposes. The thicknesses of the PDMS samples were found by using a profilometer (Bruker Dektak XT stylus Profilometer Surface Profilometer).

$$\text{Resistivity, } \rho = \frac{Rwt}{l} = Rt \quad (3)$$

Finally, to find the electrical conductivity (EC) of the samples taken directly from (Heaney, 2003), the resistivity calculated in eq. 3 is inversed by a factor of 1, as shown in eq. 4:

$$\text{Electrical Conductivity, } \sigma = \frac{1}{\rho} \quad (4)$$

These equations were used alongside excel data analysis to find and record each tested film's conductive properties.

Figures 5 and 6 exhibit non-linearity, with lots of noise in the dataset indicated by the unstable current, which consequently produces unstable resistances. Therefore, the graphs' linear regression equation was found by fitting each curve with a trendline. The equation's gradients represented the inverse resistance, was used with Eq. 2 and 3 to calculate film resistivities and ECs [7, 9].

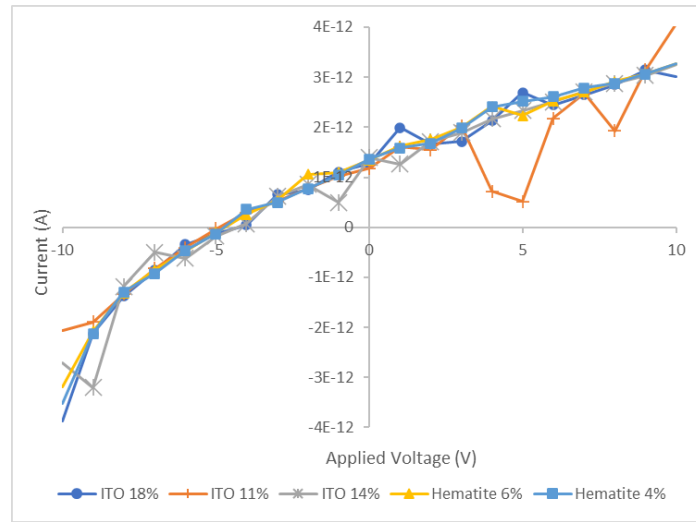


Figure 5: ITO (11-18%) and Hematite (4-6%) films tested at an applied voltage of -10V to +10V at 21 steps on an axis of current vs voltage.

To show how that resistances were found from the graphs, Figure 6 represent the process of isolating films and fitting a trendline to the curves in each applied voltage before averages were taken in Table 4.

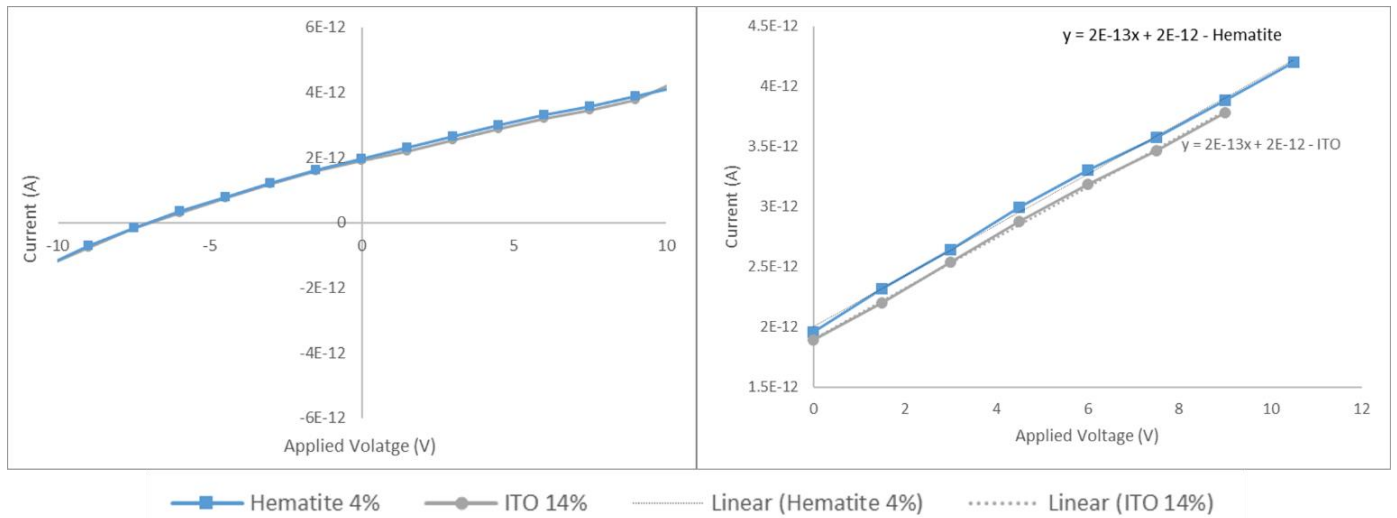


Figure 6: Films from ITO and Hematite, -10V to +10V at 21 step counts.

Table 4: calculated resistances, resistivities and electrical conductivities from the 2-point probe. Film thicknesses were found using a profilometer (Bruker Dektak XT stylus Profilometer Surface Profilometer) and recorded in the table. Box-and-whisker plots of the data were used to identify outliers in the applied voltage range and were written in red. Outlier values were excluded from the averages and standard deviations of the data sets.

ITO (18%)				
Applied voltage (V)	ITO Resistance ( $\Omega$ )	Film thickness ( $\mu\text{m}$ )	Resistivity ( $\Omega \cdot \text{cm}$ )	Electrical conductivity ( $\Omega^{-1} \cdot \text{cm}^{-1}$ )
5	3.33E+12	1.14E+02	3.80E+10	2.63E-11
10	3.33E+12	1.14E+02	3.80E+10	2.63E-11

15	3.33E+12	1.14E+02	3.80E+10	2.63E-11
20	3.33E+12	1.14E+02	3.80E+10	2.63E-11
<b>Average</b>	<b>3.33E+12</b>		<b>3.80E+10</b>	<b>2.63E-11</b>
Standard Deviation (+/-)	0.00E+00		0.00E+00	0.00E+00
<b>ITO (11%)</b>				
5	5.00E+12	1.00E+02	5.00E+10	2.00E-11
10	5.00E+13	1.00E+02	5.00E+10	2.00E-11
15	3.33E+12	1.00E+02	3.33E+10	3.00E-11
20	3.33E+12	1.00E+02	3.33E+10	3.00E-11
<b>Average</b>	<b>4.17E+12</b>		<b>4.17E+10</b>	<b>2.50E-11</b>
Standard Deviation (+/-)	8.33E+11		8.33E+09	5.00E-12
<b>ITO (14%)</b>				
5	2.00E+12	1.39E+02	2.78E+10	3.60E-11
10	5.00E+12	1.39E+02	6.95E+10	1.44E-11
15	5.00E+12	1.39E+02	6.95E+10	1.44E-11
20	5.00E+12	1.39E+02	6.95E+10	1.44E-11
<b>Average</b>	<b>5.00E+12</b>		<b>6.95E+10</b>	<b>1.44E-11</b>
Standard Deviation (+/-)	0.00E+00		0.00E+00	0.00E+00
<b>Hematite (6%)</b>				
5	3.33E+12	6.03E+01	2.01E+10	4.98E-11
10	3.33E+12	6.03E+01	2.01E+10	4.98E-11
15	3.33E+12	6.03E+01	2.01E+10	4.98E-11
20	3.33E+12	6.03E+01	2.01E+10	4.98E-11
<b>Average</b>	<b>3.33E+12</b>		<b>2.01E+10</b>	<b>4.98E-11</b>
Standard Deviation (+/-)	0.00E+00		0.00E+00	0.00E+00
<b>Hematite (4%)</b>				
5	5.00E+12	1.03E+02	5.15E+10	1.94E-11
10	1.00E+13	1.03E+02	1.03E+11	9.71E-12
15	5.00E+12	1.03E+02	5.15E+10	1.94E-11
20	5.00E+12	1.03E+02	5.15E+10	1.94E-11
<b>Average</b>	<b>5.00E+12</b>		<b>5.15E+10</b>	<b>1.94E-11</b>
Standard Deviation (+/-)	0.00E+00		0.00E+00	0.00E+00

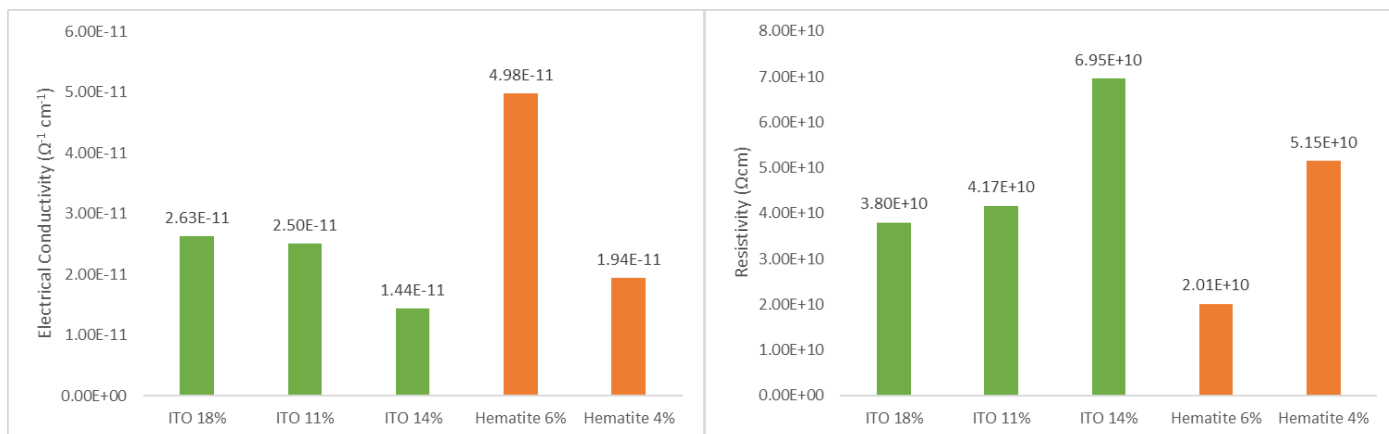


Figure 7 (above left): EC of ITO films (11-18%) and Hematite films (4-6%) compared via bar chart

Figure 8 (above right): Resistivities of ITO films (11-18%) and Hematite films (4-6%) compared via bar chart

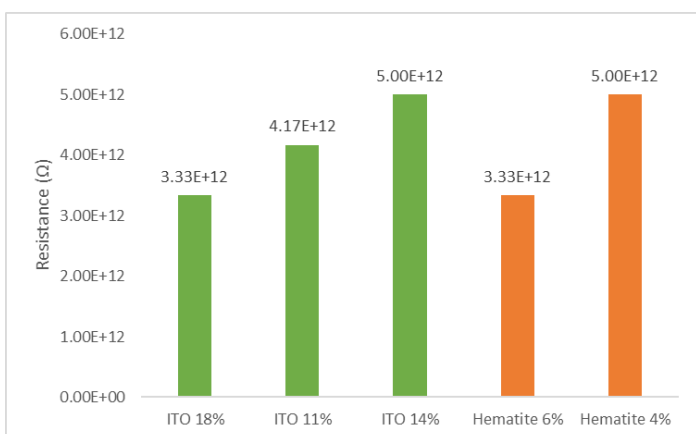


Figure 9: Comparison of films' resistances across ITO films (11-18%) and Hematite films (4-6%)

The averaged data values without outliers from Table 4 were compared via bar charts (Figures 7 to 9). From these it is seen that the 6% Hematite film had the highest conductivity at  $4.98\text{E-}11 \Omega^{-1} \text{ cm}^{-1}$  and lowest resistivity at of  $2.01\text{E+}10 \Omega \text{ cm}$ , followed by 18% ITO with a conductivity of  $2.63\text{E-}11 \Omega^{-1} \text{ cm}^{-1}$  and resistivity,  $3.80\text{E+}10 \Omega \text{ cm}$ . Comparing these film resistivities to SYLGARD®184's own volume resistivity of  $2.9\text{E+}14 \Omega \text{ cm}$  [22] shows a clear decrease in resistivity by factors of  $\sim 14000$  (hematite 6%) and  $8000$  (ITO 18%), to the nearest

thousand. Where, SYLGARD®184 's EC was then calculated using eq. 4, giving  $3.45\text{E-}15 \Omega^{-1} \text{ cm}^{-1}$ , the smallest conductivity yet.



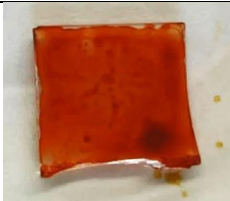
Surprisingly, the ITO film had a lower EC than hematite (6%) given that the blend contained both HNR and the conductive ITO NPs. However, this was likely due to the film containing less HNR, equivalent to hematite 4% than 6%. Therefore, comparing the ITO 18% film to hematite 4% shows that there was an increase in conductivity in the PDMS: hematite + ITO film over the PDMS: hematite film by a factor of  $\sim 1.4$ , thereby showing that the addition of conductive ITO NPs does increase the overall film conductivity. This shows that the addition of hematite and ITO, individually and together, increases the electrical conductivity of the PDMS film. However, as seen from Figure 7, the conductivities of both films (hematite 6% and ITO 18%) were extremely low with extremely high resistances (Figure 9), making them unsuitable candidates for this project's semiconductive scaffold, given our desired resistances of  $\sim 10 \text{ k}\Omega$  [23].

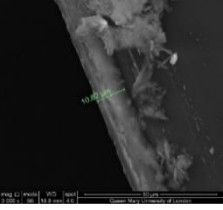
In conclusion, the quantities of hematite and ITO used in this experiment (Table 2) were too small to generate a significant EC and low resistances, so future experimentation would require larger quantities of the conductive/semiconductive additions to counteract the insulating properties of PDMS.

### 3.2. Experiment 2 – PEDOT:PSS and Hematite Film

Experiment 2 builds on the issues encountered in experiment 1 with handling SYLAGRD®184's PDMS. A potential solution to the low conductivity and high resistance films encountered in experiment 1 was to use PEDOT: PSS as a medium to disperse HNR within. PEDOT: PSS is a naturally conductive organic polymer with flexible mechanical properties used in making thin films for bioelectronic analysis purposes [12]. They can be purchased commercially in solution with low viscosities [16] making it an ideal choice to potentially generate a photocurrent with hematite.

New HNR powder was synthesised using the method in Table 3. Table 5 shows a colour change in the nanorods compared to those used in experiment 1 which was made by a previous research group member – Dr Bo Zhou. To check for the presence of hematite crystal in the red HNR powder, the sample underwent an X-Ray Diffraction (XRD) test with the resultant spectroscopy graph compared to the standard peaks of the Inorganic Crystal Structure Database's (ICSD) XRD data [8] for hematite (Figure 10) showing successful synthesis of hematite crystals with the corresponding peaks. During experimentation, both batches of red HNR powder aggregated into lumps after furnacing compared to the finer orange nanoparticle powder, despite sonicating the pre-cursor solution regularly to maintain uniform particle dispersion. Li et al., 2018 encountered this issue where their hematite precursor clustered at high furnace temperatures affecting its ability to retain its nanostructure and uniform particle dispersion in media. In experiment 2, we observed a lengthier dispersion time for red HNR dispersion in PEDOT: PSS (~1 hour sonicating) compared to dispersion in PDMS. Therefore, future synthesis should involve furnacing at lower temperature, minimum 450°C to create hematite crystals, to maintain the HNR nanostructure due to the issues with particle aggregation in the red HNR which was furnaced at 520°C.

Table 5: <i>Experimental photos from the PEDOT: PSS + hematite film fabrication (3 sig fig)</i>		
No.	Image	Description
1		Hematite nanorods
2		Dispersed Hematite nanorods in PEDOT: PSS solution, ratio of ~ 1:6. 40 µL of solution was pipetted onto FTO coated and glass slides (1.2 cm x 1.2 cm), spin-coated and cured.
3		14% hematite and PEDOT: PSS film on 1.2 cm x 1.2 cm glass square. The film is semi-transparent, fully covering the square and spin-coated well. There is a uniform distribution of the HNR across the glass, compared to previous attempts with PDMS.  Some experimental observations included surface tension of the standard glass versus the FTO layered glass after the blend was pipetted on; FTO glass had better (lower) surface tension than glass after etching with Piranha solution . After spin-coating and curing, the hematite films

4		SEM – FEI Inspec-S Scanning Electron Microscope image of the PEDOT: PSS + hematite film used to measure the film’s thickness. Uniform thickness of 10.8 µm was found across the sample.
---	---	---

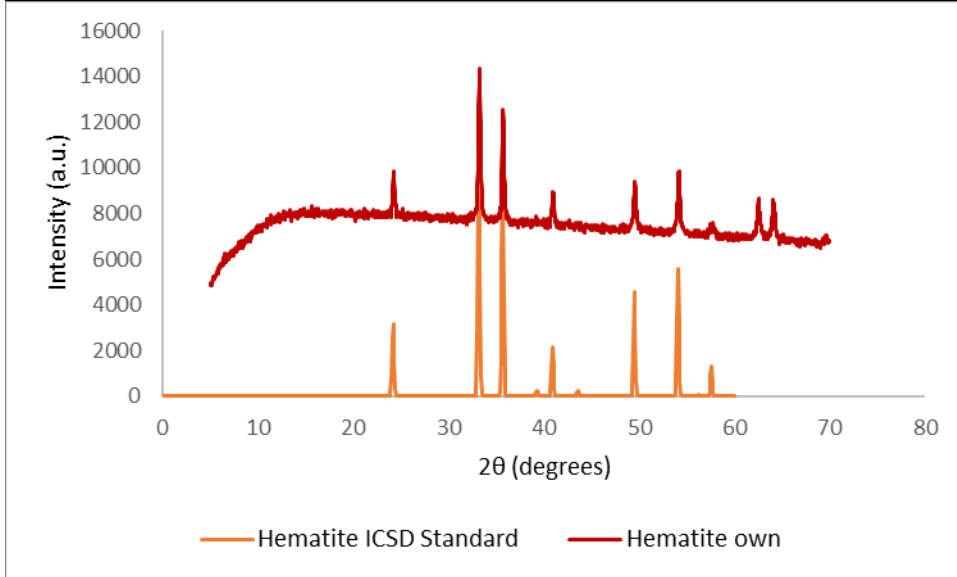


Figure 10: XRD data for the hematite used in the PEDOT: PSS and hematite film compared to a standard peak values checking if the particles contained hematite crystals or not. The comparison shows the presence of hematite crystals in the red powder tested.

A 14% Hematite PEDOT: PSS film was made (Table 2 and 3) on regular glass slides for conductivity testing with a 4-point probe and data recorded in Table 6. A film was also made on FTO coated glass for photoelectrochemical testing with linear sweep voltammetry (LSV) (Figure 15). Figures 11 and 12 display the current-voltage graphs at applied voltages of 0.1V-15V of the film measured by a 4-point probe and the corresponding

conductivity calculations using Eq. 1-5 and linear regression. The resistivity equation of a square film using a 4-point probe was taken from Heaney 2003, page 7-8 where  $h$  = film thickness,  $V$  = applied voltage and  $I$  = current generated, in eq. 5:

$$\text{Resistivity, } \rho = \frac{Vh}{I} \quad (5)$$

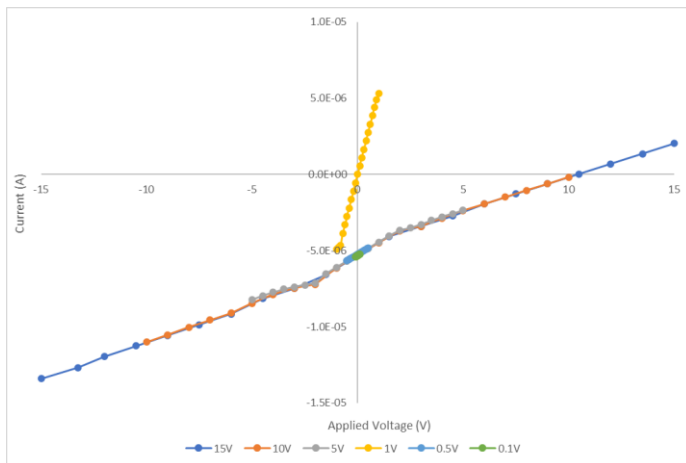


Figure 11 (0.1-15 V): 4-point probe conductivity testing of 14% hematite and PEDOT: PSS film with an applied voltage range of 0.1 V -15 V.

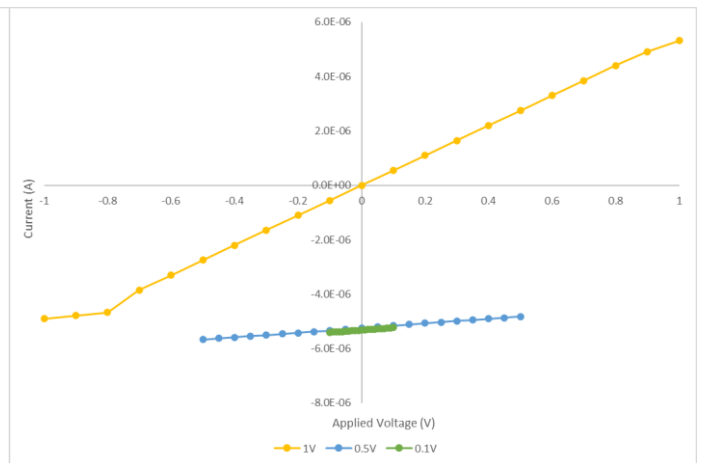


Figure 12: 4-Point probe conductivity testing of 14% hematite and PEDOT: PSS film with applied voltage range of 0.1 V-1 V, focusing on the film's behaviour at smaller voltages.

From both figures, 1V demonstrates correct ohmic behaviour where  $I = V = 0$ , compared to the voltages that show a negative current around  $-6E-06$  A at  $V = 0$ , rejecting Ohm's law (eq. 1). The graphs have a negative current, likely due

to the degenerative behaviour of the film as PEDOT: PSS is a highly sensitive and unstable material, where the high voltages applied likely killed the film resulting in the odd graphs featured. The film was tested between 1V-15V before being tested at 0.1 V-0.5V, where these large voltages were applied to maintain continuity in conductivity testing throughout all experiments in this project. However, given the non-ohmic behaviour from 5V onwards, data, it would have been best to test the film chronologically at a maximum voltage of 1V to maintain PEDOT: PSS film viability. Therefore, the values used in calculations and analysis were taken as absolutes and recorded in Table 6.

*Table 6: PEDOT: PSS and Hematite (14%) film. Outliers highlighted in Red. Thickness measured through SEM. (3 sig fig) outliers removed from final averages. Data shown in absolute value form otherwise we had negative currents, resistivities and electrical conductivities due to the odd graph behaviour. Box and whisker plots were applied to the resistance, resistivity, and conductivity data during excel analysis to identify any outliers in the data. Outlier values were excluded from the averages and standard deviations of the data sets.*

Solid composition of Hematite (%)	Film thickness (μm)	Applied Voltage (V)	Absolute Current (A)	Resistance (Ω)	Resistance (kΩ)	Resistivity, $\rho$ ( $\Omega \cdot \text{cm}$ )	Electrical conductivity, $\sigma$ ( $\Omega^{-1} \text{cm}^{-1}$ )
14.1	10.8	0.1	4.92E-06	1.25E+06	1.25E+03	2.20E+01	4.57E-02
		0.5	4.55E-06	1.11E+06	1.11E+03	1.19E+02	8.41E-03
		1	4.99E-06	2.00E+05	2.00E+02	2.17E+02	4.60E-03
		5	2.00E-06	1.67E+06	1.67E+03	2.71E+03	3.70E-04
		10	1.00E-06	1.67E+06	1.67E+03	1.08E+04	9.24E-05
		15	1.50E-06	2.00E+06	2.00E+03	1.08E+04	9.24E-05
		Average	3.16E-06	1.54E+06	1539	4.90E+03	1.09E-02
		SD	1.69E-06	3.20E+05	320	4.93E+03	1.76E-02

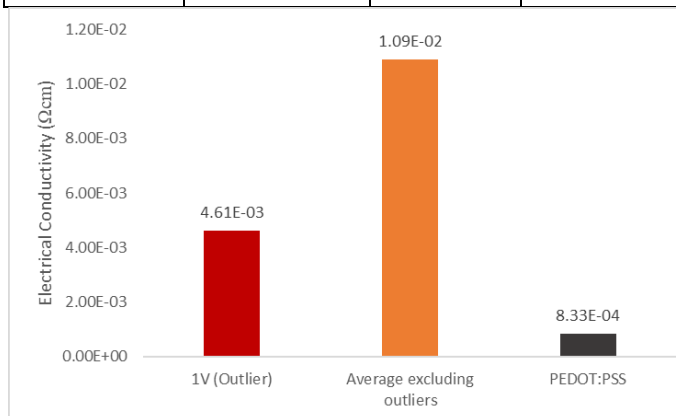


*Figure 13: ECs of PEDOT: PSS + hematite film compared to the calculates EC of PEDOT: PSS only, via bar chart*

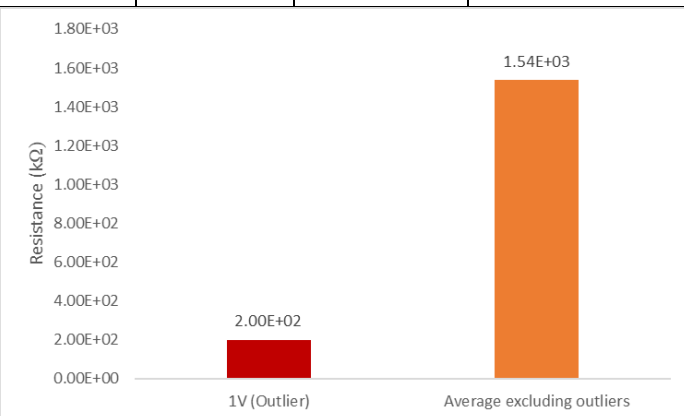


*Figure 14: Resistances of PEDOT: PSS + hematite film measured at 1V and averaged, absolute values compared via bar chart*

The commercial PEDOT: PSS solution used in this report had a resistivity of  $< 0.0012 \Omega \text{cm}$  [16] and calculated EC of  $8.33\text{E-}04 \Omega^{-1} \text{cm}^{-1}$  using eq. 4. Figure 13 shows that the average film EC had the highest electrical conductivity at  $1.09\text{E-}02$

$02 \Omega^{-1} \text{ cm}^{-1}$  followed by the 1V Outlier at  $4.61\text{E-}03$ , both of which were larger than the conductivity of only PEDOT: PSS by 172% and 139% respectively. However, given the fact that the Averaged resistivity and conductivity values were taken as absolutes due to the damaged film, the values calculated at 1V would provide a more accurate representation of the increased conductivities. And despite the Average groups' high conductivity, the film's resistance at 1V is substantially less than that of the Averaged value (Figure 14) by a percentage difference of 154% (3 sig. fig), which supports the decision to take the values at 1V as the most representative of the 14% hematite film.

The hematite percentage of this film was over double the amount used in experiment 1, producing higher conductivities and lower resistances than hematite (6%) and ITO (18%), making it suitable for photocurrent testing. The photoelectrochemical measurement set up [26] (Figure 1) was used to conduct an LSV test on the PEDOT: PSS + hematite film, at an applied voltage range of 0-1V, with a blue light source (laser) of wavelength,  $\lambda = 486 \text{ nm}$  at 10s Dark/Light intervals (Figure 15). The graph shows an increasing dark current but no photocurrent generation.

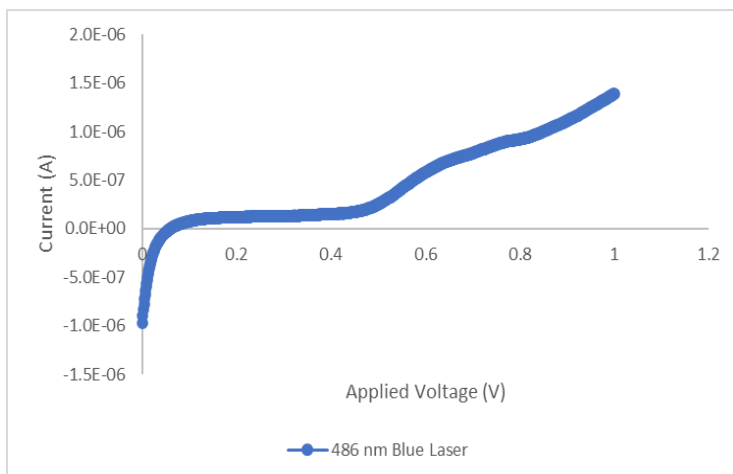


Figure 15: Current/Voltage graph of PEDOT: PSS + hematite film tested photoelectrochemically via Linear Sweep Voltammetry and collected virtually using AutoLab

One potential reason for this was PEDOT: PSS's instability and sensitivity when under intense light sources and an applied voltage, can damage the film, resulting in no photocurrent [12]. A second prospect involves issues with hematite as a material. Li et al., 2018 found that the lifetime of charge carriers in pure hematite was as small as pico-seconds in their use of hematite in water splitting. It was assumed that with this photocurrent test, electrons in the localised illuminated region were not promoted to the conduction band nor was a site of increased conductivity created and therefore, no photocurrent – spike in the increasing current – was observed (Figure 15). Charge carriers can also have high resistance when moving through semiconductors. So most photoinduced electron and holes in the electron hole pairs recombine before reaching the semiconductor bulk or surface, thereby not increasing the number of redox reactions occurring at the electrode/electrolyte interface and generating a photocurrent through the methods described in the introduction. Liao et al., 2011 found that issues like charge carrier resistance and lifetime can be solved by doping the hematite with zirconium, silicon and germanium or tin. To increase the conductivity of the semiconductor with a higher density of free electrons that can be promoted, generating a larger quantity of holes that can participate in redox reactions and the semiconductor surface, which is what Zhou et al., 2021 did with their Sn doped hematite films.

### 3.3. Experiment 3 – PDMS: ITO Concentration Series

The PEDOT: PSS + hematite film produced the highest conductivity and least resistance out of the fabricated blends. However, the sensitivity PEDOT: PSS as an organic polymer created a degeneration issue under prolonged illumination



and high voltages. Given the poor results both in conductivity and photocurrent testing, caution is needed when testing organic films which are very sensitive compared to inorganic PDMS which was able to withstand very large voltage ranges without degeneration. Therefore, based on PDMS's resistance to degradation a PDMS: ITO concentration series from 30% - 80 % was conducted to find the optimum film percentage to create an inorganic film (Table 2) with the desired conductivities and resistances of a semiconductor [23].

From Figures 16 and 17 it is observed that Hexane was not a good solvent for high concentration ITO nanoparticle films, even with plasma treating the glass surfaces, due to evaporating quickly in room temperature when used in small quantities (<40  $\mu$ L). The solvent evaporated forming a dried, crumbled, and solid mass that could not be spread over the glass when spin coated. The plasma treater was also dirty so the glass squares could have been contaminated with oil.

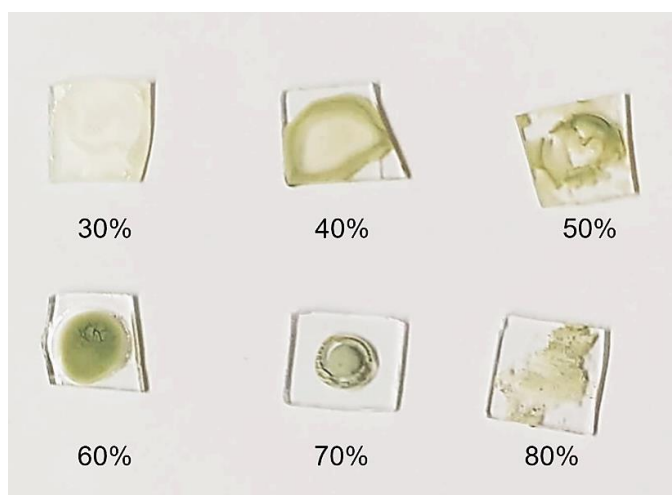


Figure 16: ITO concentration series (without carbon contacts), spin-coated film samples of SYLGAD 180 PDMS and curing pack (0.1g) dissolved in Hexane (1 mL), with varying concentrations of dispersed ITO on plasma treated 1cm x 1cm glass squares.

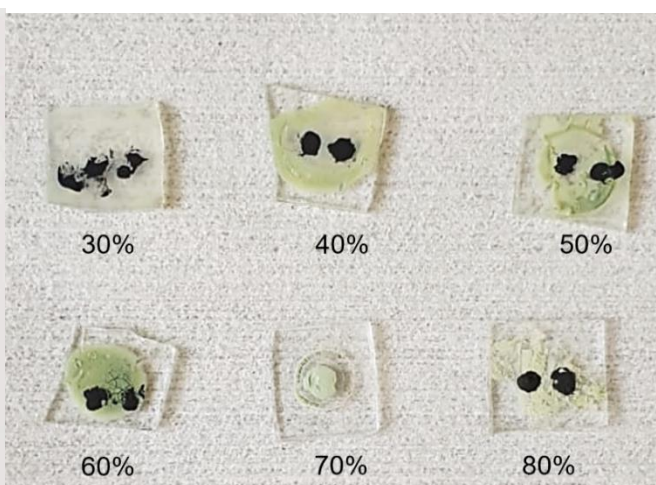
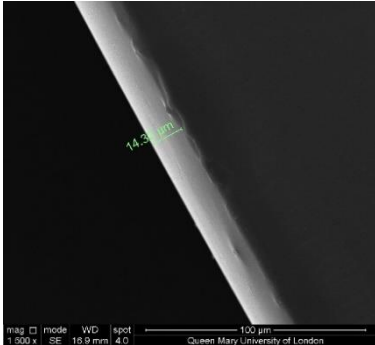
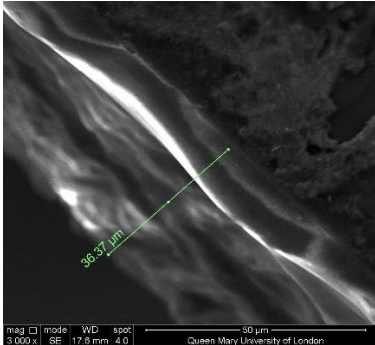
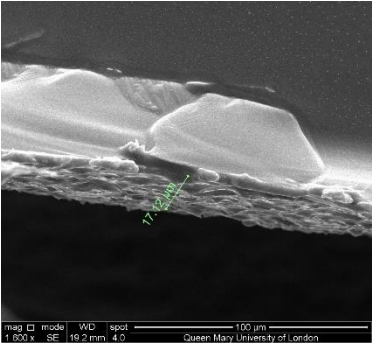
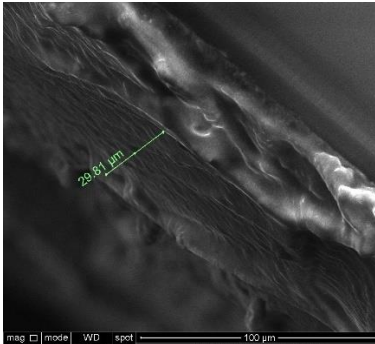
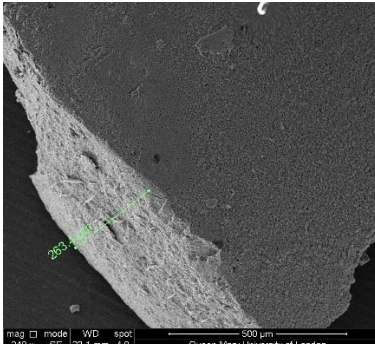
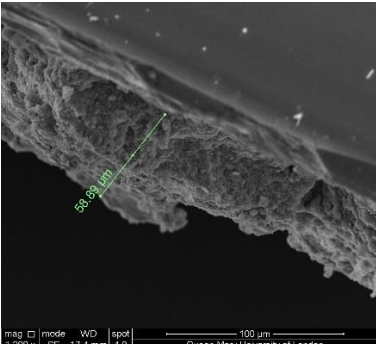


Figure 17: ITO concentration series (with carbon contacts), spin-coated film samples of SYLGAD 180 PDMS and curing pack (0.1g) dissolved in Hexane (1 mL), with varying concentrations of dispersed ITO on plasma treated 1cm x 1cm glass squares, with carbon paste contacts templated onto the films for improved electrical contact testing with the 2-point probe, barring the sample at 70% ITO composition.

Table 7: table sharing SEM images of the ITO concentration series' film thicknesses with digital measurements up to 3 sig. fig. SEM (FEI Inspec -S) using the microscope xt server to digitalise the microscope image. Averages were not taken.

		
30% - 14.32 μm	40% - 36.4 μm	50% - 17.1 μm
		
60% - 29.8 μm	70% - 263 μm	80% - 58.9 μm

From both Figure 16 and Table 7, it can be observed that the Hexane, PDMS and ITO mixtures yielded poor films, with uneven surfaces. With increasing ITO nanoparticle powder concentrations, the blends' viscosities increased until solid droplets were achieved from the 60%-80% film range.

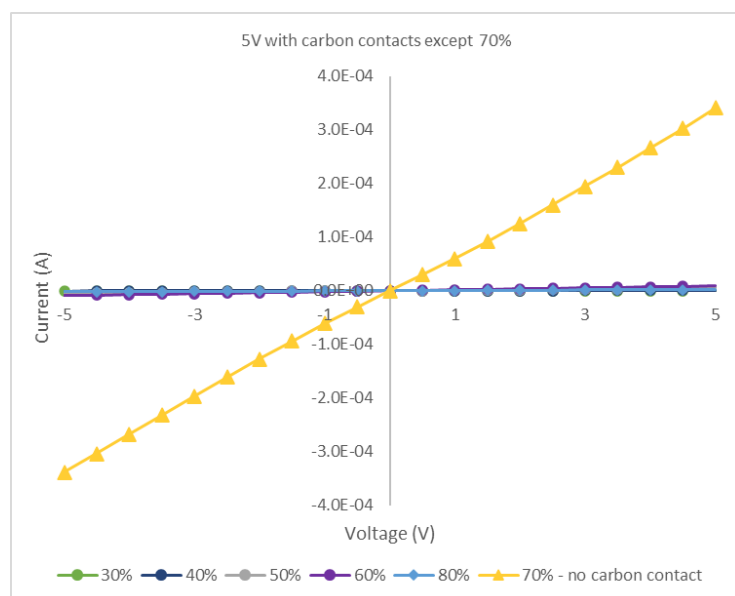
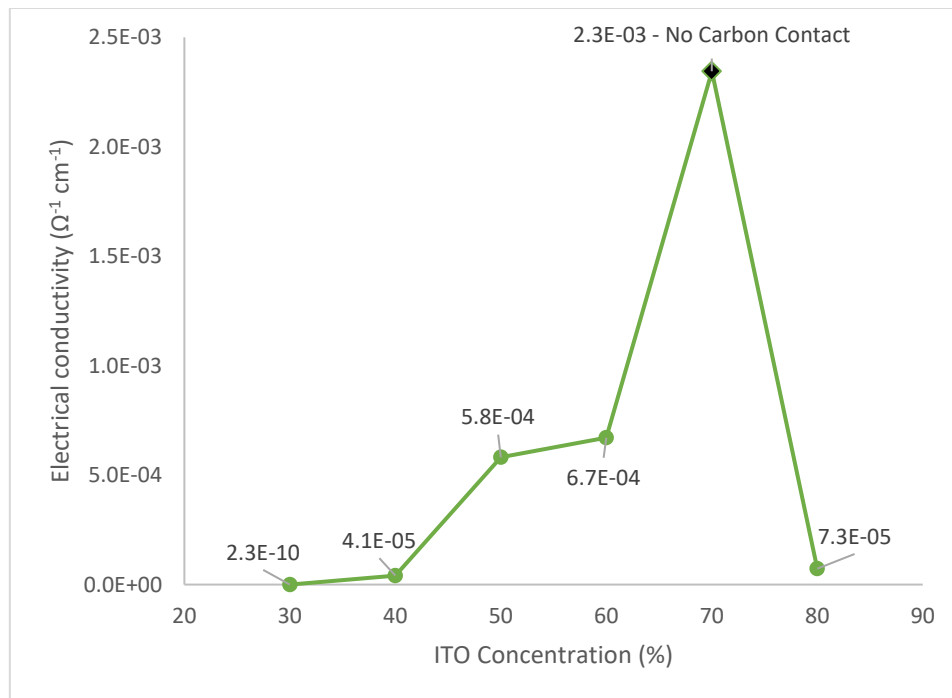


Figure 18: 5V with Carbon contacts at 21 steps.

As before, a 2-point probe was used for conductivity data and excel to analyse the curves. through curve equations were found through excel. The average resistance, resistivities and conductivities were calculated using eq. 1-4 and recorded in table 8.

*Table 8: ITO concentration series with carbon paste contacts (excluding 70%). Box and whisker plots were applied to the resistance, resistivity, and conductivity data during excel analysis to identify any outliers in the data, but none were found.*

Percentage composition of ITO (%)	Film thickness ( $\mu\text{m}$ )	Resistance ( $\Omega$ )	Resistivity, $\rho$ ( $\Omega \cdot \text{cm}$ )	Electrical conductivity, $\sigma$ ( $\Omega^{-1} \text{cm}^{-1}$ )
30	14.32	3.06E+12	4.38E+09	2.29E-10
40	36.37	6.67E+06	2.42E+04	4.12E-05
50	17.2	1.00E+06	1.72E+03	5.81E-04
60	29.81	5.00E+05	1.49E+03	6.71E-04
70 (no carbon contact)	263.4	1.62E+04	4.26E+02	2.34E-03
80	58.89	2.33E+06	1.37E+04	7.28E-05



*Figure 19: Graph of electrical conductivity calculated from Table 8 against ITO percentage concentration, comparing conductivities of each film.*

Conductive, adhesive carbon paste [9] was used to increase the contact between the probes and thin films. This decreased the resistance between the film and the probes than when the PDMS: hematite + ITO films were tested without paste [9], retrieving more accurate measurement of the films' electrical conductivities. Figure 19 shows that electrical conductivity increased with increasing concentrations of ITO. The highest conductivity at  $\sigma = 2.3\text{E-}03 \text{ } \Omega^{-1}\text{cm}^{-1}$  at the lowest film resistance of 16.2 k $\Omega$  came from the 70% film, despite not using carbon contacts, which is within the preferred resistance range of semiconductors [23]. Therefore, given the behaviour of the graph in Figure 19 and

the film's low resistance, 70% ITO film was identified as the percolation threshold where the concentration that a material changes from insulator to conductor [20].

In percolation threshold studies, a steadily increasing curve is expected with increasing concentrations of a conductive filler material, that when added to a medium like PDMS, it disperses well, forming a conductive network [20]. Ram et al. (2016) also explain that percolation theory is used to find the least amount of conducting additive, in this case ITO, required to change a material from an insulator to a conductor. This was necessary as we saw in experiment 1, where the PDMS was highly insulating so it was concluded that larger quantities of additive – ITO and Hematite - were required to make the film conducting. Unlike regular percolation curves [20], the conductivity in this ITO series decreased when testing the 80% film. This was likely due to the poor film, that had a powdered and crumbled texture of the blend likely because of the high concentration of ITO nanoparticle powder used and the hexane evaporating quickly at room temperature at small quantities [2]. The 80% film gave a solid blend that could not be uniformly distributed on the glass squares, likely ensuring that the probes contacted the glass rather than the solid sample itself, which could have resulted in a lower current than expected.

Regardless, Figure 19 showed that the percolation threshold for the ITO concentration series was at 70%. Therefore, given these results and the physical observations of the films themselves, it can be decided that a 70% ITO film is the best choice for creating a conductive film with PDMS and Hematite. In future, a hematite concentration series should be conducted to find the optimum hematite concentration with to pair with the 70% ITO and SYLGARD®184 PDMS, preferably with a better solvent than hexane, like toluene.

### 3.4. Experiment 4 – Gelatin Scaffold Templating

After reviewing different scaffold templating methods used in biomaterials research, a gelatin porogen leaching method [24] was chosen for adaptation in this research project using micro-sized gelatin particles sintered in solution to create a porous template to overlay with a semiconducting blend. Xu et al. 2020, successfully created a macroporous and spherical PDMS based scaffold which we attempted to replicate in smaller samples on glass slides.

One difference between the original scaffold method and the adaptation was scaffold size. This project aimed to make a flat 3D scaffold on flat glass compared to spherical moulds [24] which used a higher mass of particles to create an orbital implant. This larger size demands larger amounts of particle and solution mass which may have learnt to their success however scaling down the quantities meant that using the same sintering conditions (40 °C for 12 hours) melted the flat scaffolds instead. Another was scaffold size. Uniformity of the flat scaffolds was impossible without a repeatable mould like a spherical one [24] and it limited the volume of liquid applicable as the gelatin pile could not be fully submerged in solution. Finally, due to the issues with scaffold's melting when sintered in the original conditions, flat pile gelatin particles were sintered on a hot plate at varying temperatures and times, and particle sintering checked via microscope until finding the optimum temperature (60 °C) and time (20 mins) to produce a porous gelatin scaffold on flat glass (Figure 20 and 21).



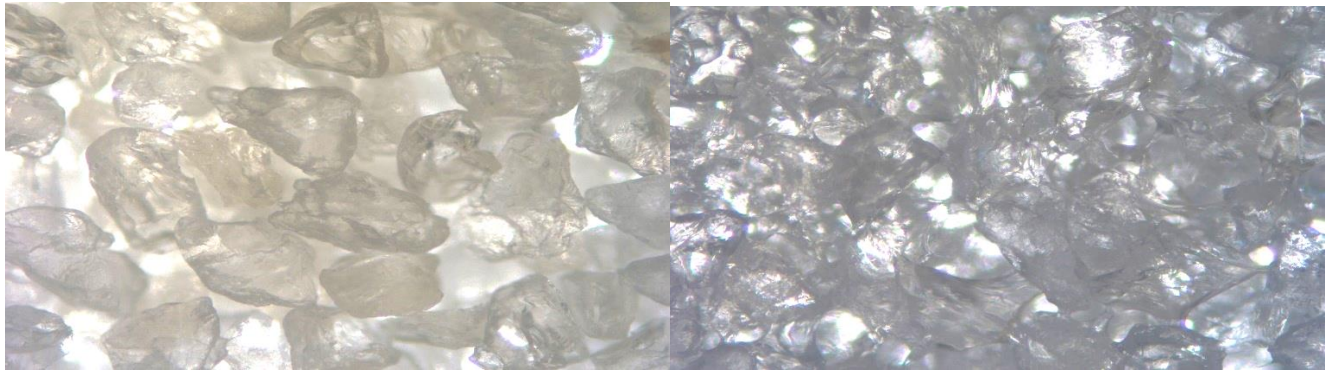


Figure 20 (above left): Light microscope image of piled dry gelatin particles at 250-300  $\mu\text{m}$ .

Figure 21 (above right): Microscope image of porous sintered gelatin particles (250-300)  $\mu\text{m}$  after saturation with 40 microlitres of ethanol solution (vol/vol 85%) with Ultra-Pure water. Sintered at 60° for 20 mins.



Figure 22 (above left): Gelatin particle piles pre-heating in oven at 40° for 8 hours

Figure 23 (above right): Gelatin, post-heating in oven at 40 for 8 hours. Particles has melted into a film instead of sintering into a scaffold

## 4. Conclusion

In conclusion, it was shown that the conductivities of PDMS and PEDOT: PSS increased with the addition of hematite and ITO at larger film percentages. Variations of hematite and PDMS based films were tested to create a semiconductive material to used in fabricating a 3D scaffold for LAE imaging. The ECs of the best samples are compared in Figure 24 with PEDOT: PSS + hematite, representing an organic film, and PDMS: ITO (70%), representing an inorganic film, performing the best in this project at  $\sigma = 4.61\text{E-}03 \Omega^{-1}\text{cm}^{-1}$  and  $2.30\text{E-}03 \Omega^{-1}\text{cm}^{-1}$  respectively. However, given that the PDMS: ITO 70% film is only less conductive than PEDOT: PSS +hematite by an approximate factor of 2, with a low film resistance of  $1.62\text{E+}04 \Omega$  and the issues with handling the organic film's sensitivity, further experiments could involve a PDMS: Hematite concentration series to find the percolation threshold. These results could be combined with the results from the 70% ITO film to create an inorganic material blend that is resistance to degradation and biocompatible, alongside experimentation with finding an ideal solvent for PDMS to dissolve in for use in spin coating.

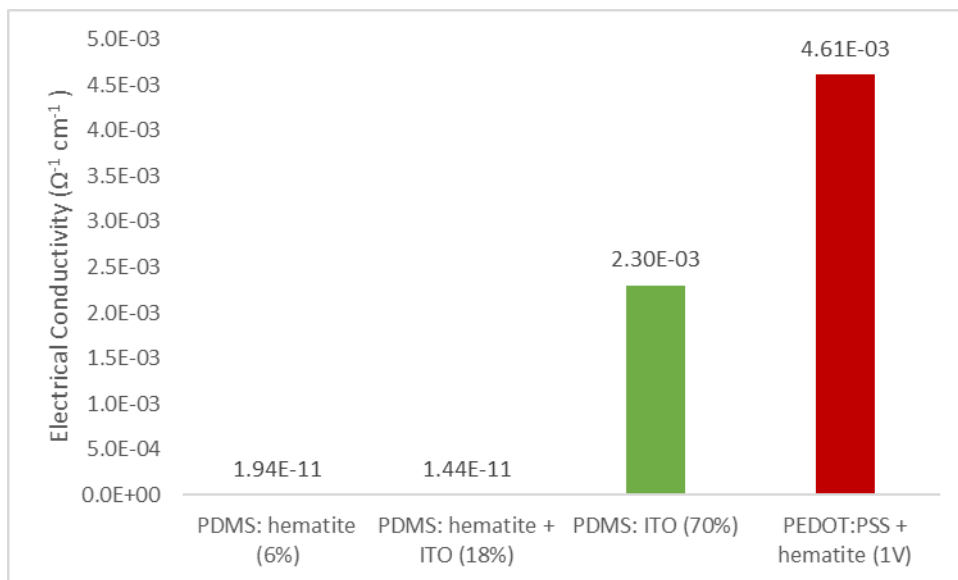


Figure 24: EC comparison via bar chart of the best performing films from experiments 1-3

Unfortunately, the data collected in this report was not robust enough to be used to generate a 3D scaffold to culture cardiomyocyte cells onto, as further experimentation is required to find an optimum semiconducting blend that will produce an efficient photocurrent and then templated into a 3D scaffold.

## Bibliography

1. Afewerki, S., Sheikhi, A., Kannan, S., Ahadian, S., & Khademhosseini, A. (2018). Gelatin-polysaccharide composite scaffolds for 3D cell culture and tissue engineering: Towards natural therapeutics. *Bioengineering & Translational Medicine*, 4(11), 96-115. doi:<https://doi.org/10.1002/btm2.10124>
2. Ashland LLC;. (2018, December 15). *Product Stewardship Summary Hexane*. Retrieved April 15, 2023, from Ashland: [https://www.ashland.com/file\\_source/Ashland/Documents/Sustainability/rc%20hexane.pdf](https://www.ashland.com/file_source/Ashland/Documents/Sustainability/rc%20hexane.pdf)
3. Chen, L., Zhou, Y., Jiang, S., Kunze, J., Schmuki, P., & Krause, S. (2010). High resolution LAPS and SPIM. *Electrochemistry Communications*, 12(6), 758-760. doi:<https://doi.org/10.1016/j.elecom.2010.03.026>
4. Conzuelo, F., Schulte, A., & Schuhmann, W. (2018). Biological imaging with scanning electrochemical microscopy. *Proc. R. Soc. A*. doi:<https://doi.org/10.1098/rspa.2018.0409>
5. CytoSmart. (n.d.). *Label-free imaging of live cells Study live cells using non-invasive & non-toxic methods*. Retrieved from Axion Biosystems: <https://cytosmart.com/resources/resources/label-free-imaging-live-cells#:~:text=Label%2Dfree%20imaging%2C%20as%20the,to%20visualize%20label%2Dfree%20cells>
6. Furey, B. J., Stacy, B. J., Shah, T., Barba-Barba, R. M., Carriles, R., Bernal, A., & Mendoza, B. S. (2022). Two-Photon Excitation Spectroscopy of Silicon Quantum Dots and Ramifications for Bio-Imaging. *ACS Nano*, 16(4), 6023-6033. doi:<https://doi.org/10.1021/acsnano.1c11428>
7. Heaney, M. B. (2003). Electrical Conductivity and Resistivity. In J. G. Webster, *Electrical Measurement, Signal Processing, and Displays* (pp. 7-1 - 7-14). Boca Raton: CRC Press.
8. Inorganic Crystal Structure Database. (n.d.). *ICSD - Basic Search and Retrieve (Code 7797)*. Retrieved from ICSD: <https://icsdoffsite.psds.ac.uk/display/list.xhtml>
9. Lei, S., Park, S. S., Micrea, D., & Sheberla, D. (2016). Measuring and Reporting Electrical Conductivity in Metal–Organic Frameworks. *Journal of the American Chemical Society*, 138(44), 14772-14782. doi:<https://doi.org/10.1021/jacs.6b09345>
10. Lenz, A., Kariis, H., Pohl, A., Persson, P., & Ojamae, L. (2011). The electronic structure and reflectivity of PEDOT:PSS from density functional theory. *Chemical Physics*, 44-51.
11. Li, C., Luo, Z., Wang, T., & Gong, J. (2018). Surface, Bulk, and Interface: Rational Design of Hematite Architecture toward Efficient Photo-Electrochemical Water Splitting. *Advanced Materials*, 30(30). doi:<https://doi.org/10.1002/adma.201707502>
12. Liang, Y., Offenhausser, A., Ingebrandt, S., & Mayer, D. (2021). PEDOT:PSS-Based Bioelectronic Devices for Recording and Modulation of Electrophysiological and Biochemical Cell Signals. *Advanced Healthcare Materials*, 10(11). doi:<https://doi.org/10.1002/adhm.202100061>
13. Liao, P., Casparay Toroker, M., & Carter, E. A. (2011, March). Electron Transport in Pure and Doped Hematite. *Nano Letters*, 11(4), 1775-1781. doi:<https://doi.org/10.1021/nl200356n>
14. Miranda , I., Souza, A., Sousa, P., Ribeiro, J., Castanheira, E. M., Lima, R., & Minas, G. (2021). Properties and Applications of PDMS for Biomedical Engineering: A Review. *J Funct Biomater*. doi:10.3390/jfb13010002
15. Nioradze, N., Ciornii, D., Kolsch, A., Gobel, G., Khoshtariya, D. E., Zouni, A., & Lisdat, F. (2021). Electrospinning for building 3D structured photoactive biohybrid electrodes. *Bioelectrochemistry*, 142. doi:<https://doi.org/10.1016/j.bioelechem.2021.107945>
16. Ossila. (2023). *PEDOT:PSS PH1000*. Retrieved from Ossila : <https://www.ossila.com/products/pedot-pss>

17. Oswald, N. (2016, September 7). *Lasers for Confocal Microscopy*. Retrieved April 24, 2023, from BiteSizeBio: <https://bitesizebio.com/30436/lasers-confocal-microscopy/>
18. Qin, K., Parisi, C., & Fernandes, F. M. (2021). Recent advances in ice templating: from biomimetic composites to cell culture scaffolds and tissue engineering. *J. Mater. Chem. B*, 9(4), 889-907. doi:DOI
19. Rajendran, D., Ramalingame, R., Adiraju, A., Nouri, H., & Kanoun, O. (2022, January 11). Role of Solvent Polarity on Dispersion Quality and Stability of Functionalized Carbon Nanotubes. *Journal of Composites Science*, 6(26). doi:<https://doi.org/10.3390/jcs6010026>
20. Ram, R., Rahaman, M., Aldalbahi, A., & Khastgir, D. (2016, November 3). Determination of percolation threshold and electrical conductivity of polyvinylidene fluoride (PVDF)/short carbon fiber (SCF) composites: effect of SCF aspect ratio. *Polymer International*, 66(4), 573-582. doi:<https://doi.org/10.1002/pi.5294>
21. St Croix, C. M., Shand, S. H., & Watkins, S. C. (2018). Confocal microscopy: comparisons, applications, and problem. *BioTechniques*, 39. Retrieved April 22, 2023, from <https://www.future-science.com/doi/10.2144/000112089>
22. The Dow Chemical Company. (2017). *Technical Data Sheet SYLGARD™ 184 Silicone Elastomer*. Retrieved April 16, 2023, from DOW: [dow](https://www.dow.com)
23. Toshiba Electronic Devices & Storage Corporation. (2023). 1. *Conductors, semiconductors, and insulators*. Retrieved April 15, 2023, from Toshiba: <https://toshiba.semicon-storage.com/eu/semiconductor/knowledge/e-learning/basics-of-schottky-barrier-diodes/chap1/chap1-1.html>
24. Xu, P., Cao, J., Feng, X., Gao, Q., Lee, S., & Ye, J. (2020). Facile fabrication of elastic, macro-porous, and fast. *Journal of Biomedical Materials Research. Part B, applied biomaterials*, 765-774.
25. Xu, Z., Gao, Y., Li, E., Wang, Y., Zhang, J., Wang, W., . . . Wang, Q. (2013). Application of a microfluidic chip-based 3D co-culture to test drug sensitivity for individualized treatment of lung cancer. *Biomaterials*, 34(16), 4109-4117. doi:10.1016/j.biomaterials.2013.02.045
26. Zhou, B., Das, A., Zhong, M., Guo, Q., Zhang, D.-W., Hing, K. A., . . . Krause, S. (2021, February 25). Photoelectrochemical imaging system with high spatiotemporal resolution. *Biosensors and Bioelectronics*, 180. doi:<https://doi.org/10.1016/j.bios.2021.113121>